2

Determination and Design of Porosity

2.1 Introduction

The porosity of a material is defined as the ratio of the volume of the pores to the total volume occupied by the solid. Since porous materials are partially composed of empty space that can be accessed by guest molecules, they are commonly described in terms of their gas uptake properties. In Chapter 1, we showed that MOF-5 exhibits permanent porosity with a specific surface area surpassing those of well-known zeolites, porous silicates, and porous carbons. Indeed, many metal-organic frameworks (MOFs) developed later exhibit ultrahigh porosity surpassing that of all other classes of porous solids. In this chapter, we provide the basics of gas adsorption and present the unique aspects of MOF chemistry that endow them with their unusual porosity.

2.2 Porosity in Crystalline Solids

The concept of porosity was proposed as early as 1896 in inorganic zeolites and was proven experimentally less than 50 years later [1]. Since then, the chemistry of zeolites (from the Greek ζέω (*zéō*), meaning "to boil" and λίθος (*líthos*), meaning "stone") has been further developed, and principles for their synthesis and characterization have been established [2]. Although the chemistry and structural diversity of zeolites is extensive, these materials are inherently limited by the number of accessible building units and the difficulty with which they can be functionalized. This is largely due to the chemical nature of their inorganic structures that are constructed from linked tetrahedral MO_4 (M = Si, Ge, Al, …) units [2a]. The incorporation of transition metal ions and organics into the backbone of zeolites has always been a desirable goal, thus giving an impetus to the discovery and development of porous metal-organic frameworks.

Porosity in coordination compounds was first observed in a series of molecular Werner-type complexes of the general formula β-$[M(PIC)_4(SCN)_2]$ ($M = Ni^{2+}$, Co^{2+}; PIC = γ-picoline; SCN = thiocyanate) [3]. The crystal structures of these compounds have empty voids between the individual complexes as a result of the

Introduction to Reticular Chemistry: Metal-Organic Frameworks and Covalent Organic Frameworks,
First Edition. Omar M. Yaghi, Markus J. Kalmutzki, and Christian S. Diercks.

Companion website: www.wiley.com/go/yaghi/reticular

sterically demanding PIC ligands [4]. Richard Barrer and coworkers showed that these materials are indeed capable of reversible uptake of gases such as nitrogen, oxygen, argon, and hydrocarbons in a zeolite-like manner. While these molecular crystals show gas uptake, cycling of uptake and release causes a decrease in porosity attributable to a phase transition of the structure into a dense nonporous form. This is not surprising, considering that the metal complexes constituting the crystal structure are held together only by weak non-covalent interactions [5]. This example brought forward the need that in order to achieve permanent porosity it is crucial to link the molecular entities by strong bonds to afford mechanical and architectural stability.

The Hofmann clathrate and related compounds discussed in Chapter 1 are capable of absorbing specific molecules from liquid phase, but no reversible uptake of gases was reported. In contrast, the adsorption of gases by Prussian blue compounds was measured to prove their permanent porosity [6]. In 1995, Dorai Ramprasad et al. demonstrated that lithium pentacyanocobaltate $Li_3[Co(CN)_5](DMF)_2$ (DMF = *N*,*N*-dimethylformamide), a crystalline ionic material, is capable of reversible uptake of oxygen at room temperature by solid-state diffusion and binding of dioxygen to cobalt in a chemisorptive fashion, and as such this material does not exhibit permanent porosity [7].

In 1997, Susumu Kitagawa and coworkers reported the high pressure (up to 36 atm) uptake of methane, nitrogen, and oxygen by a coordination network of formula $[M_2(BIPY)_3(NO_3)_4]$ [8]. Wasuke Mori and coworkers reported dicarboxlyates of copper, molybdenum, and rhodium, and it was speculated that their structures consist of 2D layers, analogous to MOF-2 [9]. The gas occlusion of Cu(BDC)(Py) (Py = pyridine) and Rh(BDC)(Py) at low temperatures and ambient pressure were investigated but no gas adsorption isotherms were recorded [9b, c]. The conditions under which these gas uptake measurements were performed do not provide the means to quantify parameters such as pore volume or surface area and therefore a proof of permanent porosity in coordination networks remained outstanding.

According to the International Union of Pure and Applied Chemistry (IUPAC) requirements, the evaluation of permanent porosity demands the measurement of at least three and preferably five or more points in the appropriate pressure range on the N_2 adsorption isotherm at the normal boiling point of liquid nitrogen. This is because all models used to describe gas adsorption in porous solids and calculate the surface areas and other measures of porosity are only valid at the boiling point of the adsorbate and for relatively low pressure. The unambiguous proof of permanent porosity in a metal-organic extended solid was first achieved with the report of reversible nitrogen adsorption measurements carried out at 77 K for MOF-2 in 1998. Since then the gas adsorption in MOFs has been studied according to the MOF-2 example, and the chemistry of MOFs was further developed to routinely provide for mechanical and architectural stability [10]. The discovery of MOF-5 ushered in the era of 3D MOFs with large accessible pore volumes and surface areas [11]. In Sections 2.3 and 2.4, we will introduce the terminology and basic principles used to describe and evaluate porosity as well as design principles for MOFs with maximized pore size, pore volume, and ultrahigh surface areas.

2.3 Theory of Gas Adsorption

2.3.1 Terms and Definitions

Adsorption phenomena and porosity have been extensively studied and their theoretical principles and experimental measurements are well established. Here, the basics of gas adsorption by porous solids are introduced and the four parameters that are used as a measure of porosity are defined. These are specific surface area, specific pore volume, porosity, and pore size (Figure 2.1).

The term "adsorption" originally denoted the condensation of gas on a flat free surface as opposed to its entry into the bulk of a solid, as in absorption [12]. However, this distinction is frequently not observed, and the uptake of fluids (gaseous or liquid) by porous materials is often referred to as adsorption or simply sorption. The latter term is used to describe both adsorption and negative adsorption (desorption) regardless of the physical mechanism involved [13]. The exposure of a porous solid to a gas in a closed space at a definite pressure results in the adsorption of the gas (adsorbate) by the solid (adsorbent). This leads to an increase of the weight of the solid and consequently, a decrease in the gas pressure. An overview of the terminology and nomenclature used with respect to gas sorption in porous solids is given in Table 2.1.

According to IUPAC, porous materials are divided into three classes based on their pore size: (i) the term "microporous" refers to pore diameters smaller than 2 nm, (ii) "mesoporous" to pore sizes between 2 and 50 nm, and (iii) "macroporous" to pores larger than 50 nm in diameter (Figure 2.2) [14]. MOFs typically have pores within the micro- and mesoporous regimes.

2.3.2 Physisorption and Chemisorption

The interactions between the adsorbate and the adsorbent can be of physical (physisorption) or chemical (chemisorption) nature. Even though physisorption

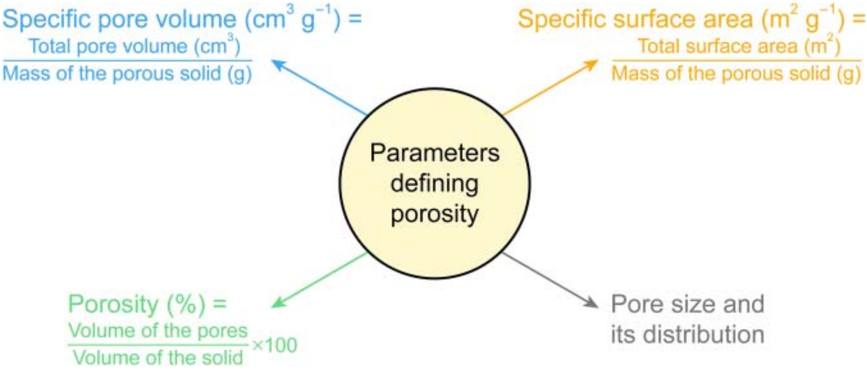

Figure 2.1 Parameters used to define porosity. The specific pore volume and the porosity are calculated from crystal structure data or density measurements. The specific surface area and the pore size distribution are estimated from adsorption data collected at the boiling point of the respective adsorbent.

Table 2.1 Terminology and nomenclature for gas adsorption.

Term	Definition
Adsorption	Enrichment of one or more components at or near an interface
Desorption	Reverse of adsorption
Adsorbent	Solid material onto which adsorption occurs
Adsorption	Absorbable substance in the fluid phase (i.e. gas or liquid)
Adsorbate	Substance in the adsorbed state
Chemisorption	Adsorption involving strong chemical interactions (e.g. chemical bonding)
Physisorption	Adsorption involving weak physical interactions
Porous solid	Solid with cavities which are deeper than wide
Open pores	Cavity or channel that can be accessed from the surface
Closed pores	Cavity or channel that cannot be accessed from the surface
Interconnected pore	Pore which is connected to neighboring pores
Blind pore/dead end pore	Pore with only one opening that connects to the surface
Interparticle space	Space between individual microscopic particles
Interparticle condensation	Condensation of adsorbent in the interparticle space
Pore size	Largest geometrical pore width, without penetrating the van der Waals radius of the atoms framing the pore
Micropore/microporous	Pores with an internal diameter < 2 nm
Mesopore/mesoporous	Pores with an internal diameter between 2 and 50 nm
Macropore/macroporous	Pores with an internal diameter > 50 nm
Nanopore/nanoporous	Pores with an internal diameter ~ 100 nm
Pore volume	Experimentally determined volume of the pores
Porosity	Pore volume/sample volume ($\text{cm}^3\ \text{cm}^{-3}$)
Total porosity	(Void volume + pore volume)/sample volume ($\text{cm}^3\ \text{cm}^{-3}$)
Open porosity	(Void volume + open pore volume)/sample volume ($\text{cm}^3\ \text{cm}^{-3}$)
Surface area	Surface accessible by an adsorbate under steady-state conditions
External surface area	Area of the surface excluding the pores (often only excluding micropores)
Internal surface area	Area of the surface of all pore walls (often only of micropores)
Monolayer capacity	Amount of physisorbed adsorbent needed to cover the surface with a monolayer or amount of chemisorbed adsorbent needed to occupy all surface sites
Surface coverage	Adsorbed substance/monolayer capacity
True density	Density of the solid excluding the pores and voids
Apparent density	Density including closed or inaccessible pores

Figure 2.2 Classification of pore sizes according to IUPAC in microporous (<2 nm), mesoporous (2–50 nm), and macroporous materials (>50 nm) along with examples listed for the respective sizes.

is an exothermic process, the interactions involved are generally weak and of a similar magnitude as those responsible for the condensation of vapors and deviations from the ideal gas behavior in real gases. Owing to the relatively low degree of specificity and directionality, physisorbed molecules retain their identity (minor changes in bond angles due to partial orbital overlap can occur) and multilayers can be formed at high relative pressures. The equilibrium in physisorption systems is generally attained rapidly but may be limited by a slow rate-determining transport process.

Chemisorption involves interactions of the same order of magnitude as those occurring during chemical reactions and the formation of chemical bonds. The highly directional nature of these interactions results in strong binding of adsorbate molecules to reactive sites on the surface that is often accompanied by surface reactions (e.g. dissociation) and a concomitant loss of identity of the adsorbate. Accordingly, chemisorbed molecules are confined to a monolayer, in contrast to the multilayer adsorption commonly observed for physisorption. Chemisorption is an activated process and hence at low temperature the system may not have sufficient thermal energy to initiate this process, resulting in slow equilibration.

2.3.3 Gas Adsorption Isotherms

Tens of thousands of gas adsorption isotherms measured on a large variety of solids are found in the literature of porous materials. Most isotherms of porous solids are due to physical adsorption and IUPAC has defined six types of isotherm: Types I to VI as depicted in Figure 2.3[1] [15], In this classification, the isotherms are distinguished based on adsorbents that are microporous (Type I), nonporous or macroporous (Types II, III, and VI), or mesoporous (Types IV and V) [14a, 16]. The relatively rare Type VI isotherm is also called stepped isotherm and is often found for nonporous materials with very uniform surfaces and is therefore mainly of theoretical interest.

The desorption process does not always proceed in exactly the reverse pathway of the adsorption, and oftentimes hysteresis (lower branch represents the

---

[1] These isotherms have been originally classified by Brunauer, Deming, Deming, and Teller, but they are most often referred to as BET isotherms after Brunauer, Emmett, and Teller. The multistep isotherm was not included in this classification.

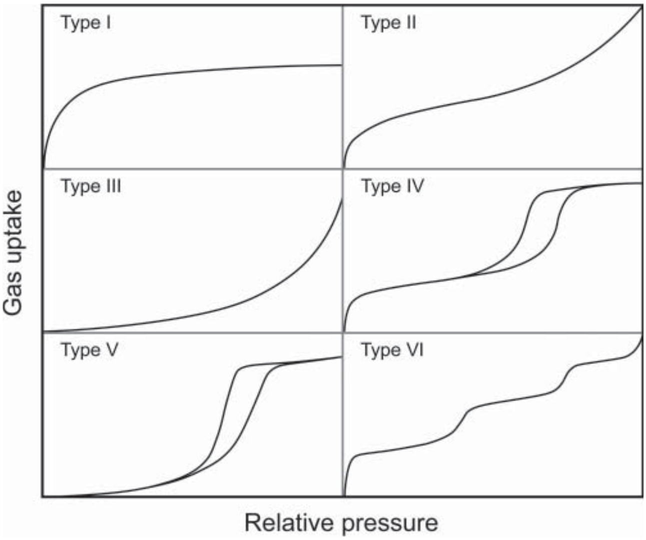

Figure 2.3 IUPAC classification of adsorption isotherms for microporous (Type I), nonporous or macroporous (Types II, III, and VI), or mesoporous (Types IV and V) materials [14a, 16].

adsorption, the upper branch the desorption process) is observed. Isotherms of Types IV and V show hysteresis and it is widely accepted that the shape of the hysteresis loop and the texture of a porous material (i.e. pore size distribution, pore geometry, and connectivity) can be correlated. IUPAC has defined four types of hysteresis that are typically observed for Type IV and V isotherms (Figure 2.4). A hysteresis of Type H1 is typically observed for materials with well-defined cylindrical pores or agglomerates of approximately uniform spheres. Materials with a wide distribution of pore sizes show Type H2 hysteresis, which can also be indicative of bottleneck constrictions. Narrow slit pores result in Type H3 hysteresis similar to that observed for nonrigid aggregates of plate-like particles, and Type H4 hysteresis is associated with wide slit pores within the material. The low-pressure hysteresis, represented by the dashed lines, can be ascribed to a change in volume of the adsorbent (the swelling of nonrigid pores) or irreversible gas uptake, which is observed when the pores are of about the same width as that of the adsorbate molecules.

In Figure 2.5, the process of gas adsorption is schematically illustrated for a porous material whose structure contains three types of pore (micro-, meso-, and macropores), correlating the gas uptake with the appearance of the gas adsorption isotherm. In the low-pressure region only little gas is adsorbed on the inner surface and this is the case for all three pore types independent of their size, as well as for the outer surface of the adsorbent (Figure 2.5a). As the pressure is increased, a monolayer is formed, covering the whole surface of the adsorbent. Simultaneously, the micropore is filled completely, resulting in a plateau in the corresponding isotherm (Figure 2.5b). A similarly shaped isotherm, indicating "mircopore filling," can thus be observed in the absence of micropores, unless

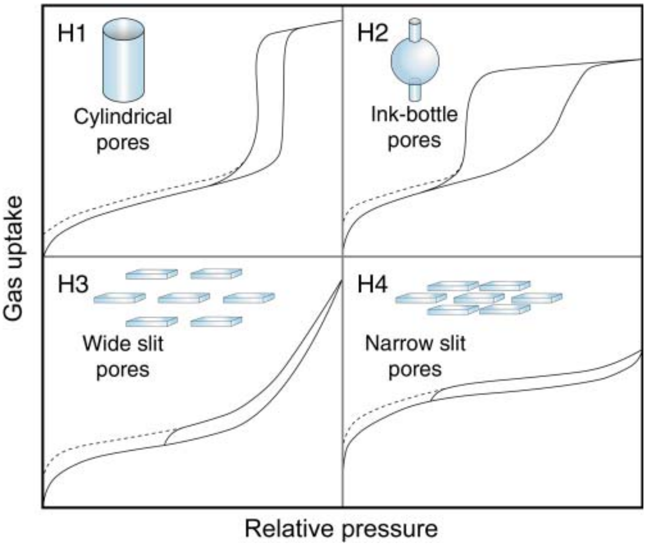

Figure 2.4 Definition of hysteresis for Type IV and V isotherms according to IUPAC. A certain shape of the hysteresis loop is commonly associated with the texture of the porous material. H1 is observed for materials containing cylindrical pores, H2 is indicative of bottleneck restrictions, and H3 and H4 are commonly observed for materials with narrow and wide slit pores, respectively.

repulsive forces between the adsorbent and the adsorbate dominate. A further increase in pressure is necessary to achieve multilayer adsorption and “mesopore filling,” which leads to a second steep ascent in the adsorption isotherm (Figure 2.5c). Similarly, a third ascent is observed, when the appropriate pressure is reached to facilitate filling of the macropores (Figure 2.5d). It should be noted, that an adsorption behavior like that of a meso- or macropore can also result from interparticle condensation, hence one must be careful when interpreting isotherm data. From the preceding discussion it has become clear that at lower pressures the uptake of gas is mainly governed by the surface area because only then the surface of the adsorbent is covered with adsorbate molecules (monolayer adsorption) while the rest of the free pore volume does not significantly contribute to the uptake.

2.3.4 Models Describing Gas Adsorption in Porous Solids

Two models are commonly used to describe adsorption phenomena in porous solids (Figure 2.6). The Langmuir model describes the surface specific adsorption involving strong forces and (sometimes) surface reactions such as the dissociation of H_2 on a Pt surface and subsequent binding as two H atoms. The Brunauer–Emmett–Teller (BET) model is applicable to cases where weak nondirectional interactions result in the non-surface-specific adsorption in the absence of surface reactions, as exemplified by H_2 molecules being adsorbed on the surface of a MOF and bound by only van der Waals interactions. The gas adsorption

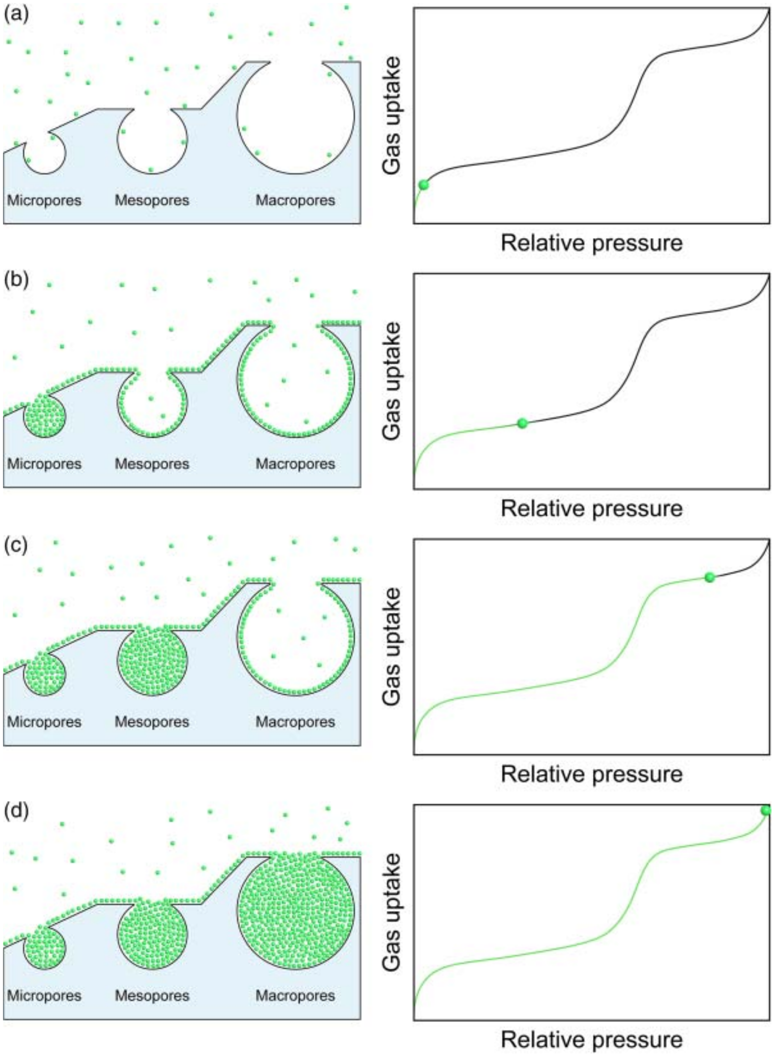

Figure 2.5 Adsorption process for a material containing micro-, meso-, and macropores. (a) In the low-pressure region, the adsorption is mainly governed by the surface area, and (b) at slightly higher pressures micropore filling is observed. (c) A further increase in pressure affords the filling of the mesopores, and (d) ultimately, when pressures close to the bulk saturation pressure are reached, to macropore filling.

in MOFs is typically governed by weak interactions (physisorption) and can, with some limitations, be described by both models. It should be noted that the main difference between them is that unlike the Langmuir model, the BET model takes into account multilayer adsorption, which is particularly important when dealing with larger pores (>2 nm).

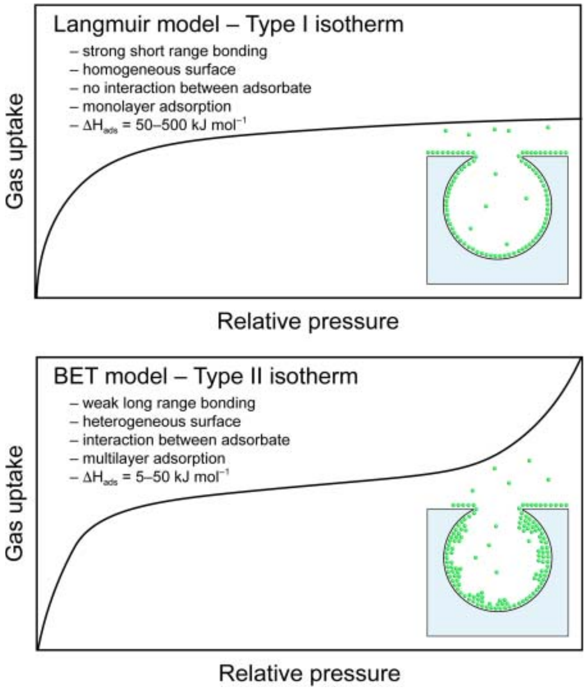

Figure 2.6 Comparison of the Langmuir and BET models for adsorption. The Langmuir model assumes strong directional adsorption (chemisorption) on surfaces in the form of monolayers, whereas the BET model assumes weak nondirectional adsorption (physisorption) and can be used to describe multilayer adsorption.

2.3.4.1 Langmuir Model

The Langmuir model is based on the idea of a limited number of adsorption sites [17]. There are multiple possible scenarios with this model: the presence of (i) only one kind of adsorption site, (ii) more than one kind of adsorption site, (iii) an amorphous adsorbing surface providing a continuum of (different) adsorption sites, (iv) sites that can accommodate more than one adsorbate molecule, (v) dissociative adsorption, and (vi) multilayer adsorption. Commonly, the Langmuir model refers to the first case: adsorption on a plane surface with only one kind of adsorption site, where each adsorption site can hold only one adsorbate molecule. This assumption highlights that this model initially did not allow for either porosity or physisorption, both present in the adsorption of gas in porous solids. Nevertheless, this model can be applied (with some restrictions) to describe gas adsorption in porous solids. Additionally, it supplies the basis on which more refined models, such as the BET model, were developed and it is therefore instructive to briefly discuss how the Langmuir model is derived [17, 18].

The Langmuir equation is derived from kinetic considerations of the adsorption process. The surface of the adsorbent is represented by an array of N^s equivalent and independent adsorption sites that can only adsorb one molecule per site. The fraction θ of sites occupied by a number N^a of adsorbed molecules is calculated following Eq. (2.1):

$$\theta = \frac{N^s}{N^a} \tag{2.1}$$

From the kinetic theory of gases, we know that the rate of adsorption is dependent on the pressure and the number of unoccupied adsorption sites (1 − θ), and the rate of desorption is dependent on the number of occupied sites (θ) and the activation energy E_A (positive energy of adsorption). The equilibrium is obtained when both the rate of adsorption and desorption are equal as described by Eq. (2.2):

$$\theta = \frac{\mathrm{d}N^\mathrm{a}}{\mathrm{d}t} = \alpha p(1-\theta) - \beta\theta \mathrm{e}^{\left(\frac{-E_\mathrm{A}}{\mathrm{RT}}\right)} = 0 \tag{2.2}$$

where α and β are constants for a given gas–solid system. Under the presumption, that in the ideal case the probability of adsorption and desorption are independent of the surface coverage (no adsorbate–adsorbate interactions) and the activation energy E_A (heat of adsorption) is constant for a given set of adsorbate and adsorbent, we can rearrange and simplify to obtain the well-known Langmuir isotherm equation

$$\theta = \frac{bp}{1+bp} \quad \text{with} \quad bp = K\mathrm{e}^{\left(\frac{-E_\mathrm{A}}{\mathrm{RT}}\right)} \tag{2.3}$$

where b is the adsorption coefficient and the pre-exponential factor K is equal to α/β, the ratio of the adsorption and desorption coefficients. For low coverage ($\theta \to 0$), Eq. (2.3) can be reduced to Henry's law, and at high coverage ($\theta \sim 1$) a plateau is reached, corresponding to monolayer adsorption. Considering the assumptions used to derive the Langmuir model, it is only strictly applicable to chemisorption. Three prerequisites must be fulfilled in order to render the Langmuir model applicable: (i) the isotherm should have a linear region at low pressures and show a plateau for $\theta \to 1$, (ii) the energy of adsorption should be independent of surface coverage, and (iii) the differential entropy of adsorption should vary in accordance with the ideal localized model [19]. These considerations indicate that the Langmuir model is not applicable to real physisorption systems even though it is commonly used to determine the surface area of porous materials. This finding is attributed to the fact that many adsorption isotherms show a shape similar to that expected from the Langmuir model (Type I). It should however be pointed out that most Type I isotherms reported in the literature are associated with micropore filling rather than monolayer coverage, and therefore the surface areas calculated using the Langmuir model are often overestimated and should be confirmed using more applicable methods such as the BET method.

2.3.4.2 Brunauer–Emmett–Teller (BET) Model

The BET model is based on the observation that physisorption is not restricted to monolayer coverage if the relative pressure P/P_0 exceeds a certain value. Accordingly, the beginning of the almost linear section of a Type II isotherm (B in Figure 2.7) was concluded to be the point likely to correspond to the monolayer completion. This is supported by experimentally determined surface areas calculated at different points (A, B, C, and D in Figure 2.7) from isotherms measured for the adsorption of several different gases, including N_2 and Ar, at or near their respective boiling points. The best agreement between the various values is found for point B indicating that at this point the monolayer adsorption

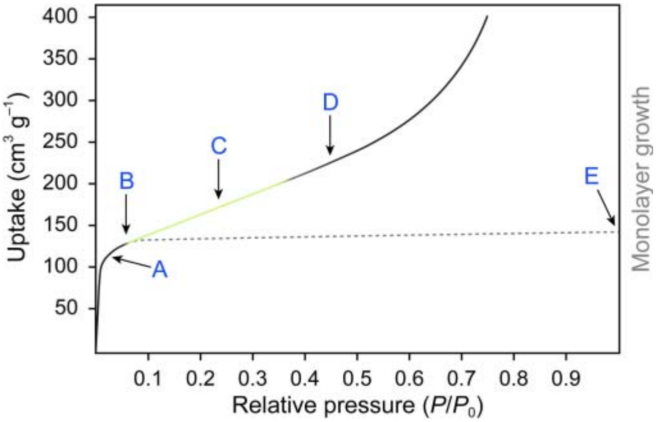

Figure 2.7 Schematic representation of the adsorption of N_2 on an Fe/Al_2O_3 surface at 77 K (black). The gray line represents an isotherm showing only monolayer adsorption. The beginning of the linear part of the isotherm (point B, linear part is highlighted in green) indicates the completion of a monolayer, as evidenced by surface areas calculated at point B from isotherms of different gases.

is complete. These findings are supported by a notable decrease of the heat of adsorption near point B.

The introduction of a few additional assumptions to the Langmuir model yields an extension of the adsorption mechanism that allows for multilayer adsorption. The resulting BET equation describes a Type II isotherm. The original BET model is an extension of the Langmuir kinetic theory that considers the formation of an infinite number of adsorbed layers at the saturation pressure (P_0). This implies that adsorbed molecules themselves can act as adsorption sites at any pressure $P < P_0$. Accordingly, the adsorbed layer is envisaged to be made up of random stacks of molecules rather than a layer of uniform thickness, where fractions of the surface are covered ($\theta_0, \theta_1, \theta_2, \theta_3, \ldots, \theta_i$, where θ_0 is the fraction of unoccupied sites) by 0, 1, 2, …, i layers. Under the assumption that in equilibrium at pressure P the fractions of both bare (θ_0) and covered (θ_i) surface are constant, the rate of adsorption and desorption for a single layer can be given by Eq. (2.4)

$$a_1 p\theta_0 = b_1\theta_1 e^{\left(\frac{-E_{A1}}{RT}\right)} \tag{2.4}$$

where a_1 and b_1 are the adsorption and desorption constants, and E_{A1} is the heat of adsorption for the first layer. This only holds true for the absence of lateral adsorbate–adsorbate interactions. Treating all possible layers the same way and assuming that (i) the sum of all θ_i equals 1, (ii) the energy of adsorption E_{Ai} equals the liquefaction energy for all layers with $i \geq 2$, and (iii) the multilayer has infinite thickness at $P = P_0$ we can derive Eq. (2.5)

$$\frac{n}{n_m} = \frac{c\left(\frac{P}{P_0}\right)}{\left(1-\frac{P}{P_0}\right)\left(1-\frac{P}{P_0}+c\left(\frac{P}{P_0}\right)\right)} \tag{2.5}$$

where n is the total amount of adsorbed gas, n_m is the amount of gas adsorbed within the monolayer, and c is a constant. A plot of n/n_m against P/P_0 at constant

c ($c > 2$), gives a curve of Type II shape, where the shape of the knee near $n/n_\mathrm{m} = 1$ is dependent on the value of c. Larger c values ($c \sim 80$) result in a sharper knee, whereas positive values of $c < 2$ result in the disappearance of the inflection point and a Type III isotherm. Rearrangement of Eq. (2.5) gives the "linear transformed BET equation" (Eq. (2.6)), which provides the basis for the analysis of experimental isotherm data in the form of the "$P/n(P_0{-}P)$ versus P/P_0 BET plot":

$$\frac{P}{n\,(P_0 - P)} = \frac{1}{n_\mathrm{m}c} + \frac{c-1}{n_\mathrm{m}c} \times \frac{P}{P_0} \tag{2.6}$$

As discussed above there is more than one model for the determination of the surface area from experimental isotherms. The most commonly used model is the BET model, originally developed to describe the multilayer adsorption on free flat surfaces, which is not the case for MOFs whose large inner surfaces are far from flat. Therefore, it was long argued whether it was valid to use this method for the determination of the surface areas of MOFs and only recently theoretical calculations made it clear that the BET model yields truly meaningful data [20]. Similar discussions were launched regarding the nonlocal density functional theory (NLDFT) models used to calculate pore sizes and their distribution. These models were also developed for materials that are substantially different from MOFs; however, the fact that good agreement between geometrically determined pore sizes and those determined from isotherms using NLDFT methods is often observed has helped to overcome these concerns. In conclusion, the choice of a suitable model to evaluate experimental gas adsorption data is crucial to obtaining meaningful values of all parameters calculated therefrom.

2.3.5 Gravimetric Versus Volumetric Uptake

A quantitative description of gas sorption is given by an adsorption isotherm: the amount of gas adsorbed by a material at a constant temperature as a function of pressure. This is expressed in either volumetric ($\mathrm{cm^3\,cm^{-3}}$, $\mathrm{g\,cm^{-3}}$) or gravimetric ($\mathrm{g\,g^{-1}}$, $\mathrm{cm^3\,g^{-1}}$, or wt%) uptake, the former being the more commonly used in the literature. The adsorption behavior is strongly dependent on the size and shape of the pores, and therefore IUPAC conventions for classifying pore sizes and gas sorption isotherms that reflect this relationship have been proposed [14]. Having introduced the terminology and the principles underlying the adsorption of gases by porous solids, we will elucidate methods to deliberately maximize the pore size and surface area of MOFs by design.

2.4 Porosity in Metal-Organic Frameworks

2.4.1 Deliberate Design of Pore Metrics

Section 2.3 illustrated that the pore shape and especially the pore size have a direct impact on the sorption properties. It has been an outstanding challenge in the synthesis of solid-state materials to alter the metrics and functionality of a given structure without changing its underlying topology. This works in MOF chemistry, where elongation or functionalization of the linker without modifying its general shape and connectivity results in the formation of isoreticular frameworks: frameworks with different pore size or functionality but the same underlying topology as the parent structure. Isoreticular structures are achieved because of *a priori* knowledge of the synthetic conditions under which the targeted secondary building unit (SBU) is formed. The successful implementation of this strategy was first demonstrated with the report of an isoreticular series of structures based on MOF-5. Here, a variety of ditopic carboxylate linkers is reticulated with Zn^{2+} ions under conditions closely related or identical to those used in the synthesis of the parent MOF-5, also termed IRMOF-1 [21]. This yields frameworks of the same general structure but with either added substituents or altered pore sizes (Figure 2.8). The expansion of linkers in the primitive cubic system may however result in interpenetrated frameworks, and in fact, for the isoreticular series of MOF-5 only the functionalized H_2BDC and 2,6-H_2NDC linkers form non-interpenetrated frameworks, whereas structures based on further expanded linkers (H_2BPDC, H_2HPDC, H_2PDC, and H_2TPDC; IRMOF-9, IRMOF-11, IRMOF-13, and IRMOF-15, respectively) form twofold interpenetrated structures [21, 22]. The non-interpenetrated forms of members of the isoreticular metal-organic framework (IRMOF) series with pore diameters of up to 28.8 Å (IRMOF-16) are prepared from more dilute solutions of starting materials. Another way to avoid interpenetration when aiming for larger pore sizes is to target structures whose topologies do not allow it, as we will discuss below.

Interpenetration of frameworks is experimentally observed for certain topologies but not for others. The potential of a structure to exhibit the phenomenon of interpenetration is assessed by considering the type of net and the open space encompassed by a structure. To describe the open space within a structure we use an approach based on nets as tilings. Tilings are polyhedra that fill the internal open space within a net (see Chapter 18) [23]. By inserting new vertices in the centers of each tile and connecting them with new edges passing through the faces of the tiles, we create a new net within the first net, and we call this the dual net. A net is termed self-dual when the interpenetrating nets are identical and a hetero-dual when they are of different topology (Figure 2.9).

It is important to note, that interpenetrating frameworks are only linked by mechanical not chemical bonds, they are entangled. Consequently, in the first step in the design of MOFs with exceptionally large pores, it is helpful to select hetero-dual nets as the product of the reticular synthesis, as these are less likely to form interpenetrated structures.[2]

For the design of MOFs with large pore sizes simple geometric consideration can be used to derive the ideal pore symmetry. Equation (2.7) describes the

---

[2] Information on whether interpenetrated nets of a certain topology exist or not can be found in the RCSR database (http://rcsr.anu.edu.au/).

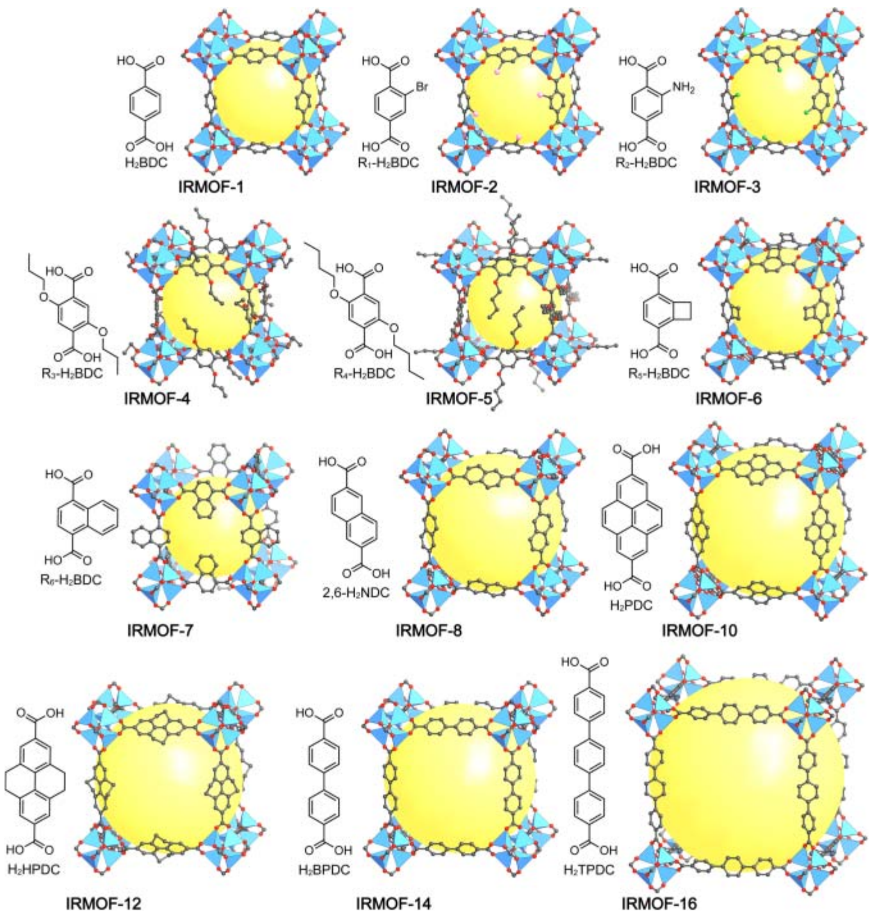

Figure 2.8 Isoreticular metal-organic framework (IRMOF) series based on MOF-5 (also termed IRMOF-1). H_2BDC derivatives decorated with various substituents yield isoreticular functionalized frameworks, and employing expanded linkers gives isoreticular expanded frameworks, both of **pcu** topology. The linkers used in the synthesis of these frameworks are shown next to the respective IRMOF structure. Only the non-interpenetrated structures are shown and all hydrogen atoms are omitted for clarity. Color code: Zn, blue; O, red; C, gray.

relation between the radius of the inscribed circle of a polygon (r) and the length of its edge:

$$r = \frac{a}{2}\cot\left(\frac{180^\circ}{n}\right) \tag{2.7}$$

where a is the length of the edge (link) and n is the number of edges. Accordingly, for a given length a of the linker the inscribed circle is larger the more corners the polygon has (Figure 2.10). By selecting a MOF with hexagonal channels that crystallizes in a net that is not prone to interpenetration, it should therefore be possible to achieve very large pore diameters while using comparatively short linker molecules.

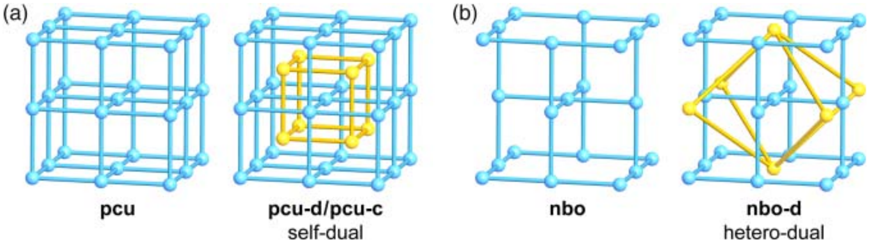

Figure 2.9 Dual nets of the **pcu** (a) and **nbo** (b) net. (a) The **pcu** net forms a "self-dual" net, meaning the dual net (yellow) has the same topology as the original one (blue). (b) In contrast, the dual (yellow) of the **nbo** net is not of the same topology as the original one (blue) and is hence termed "hetero-dual." From this consideration, it is clear that a given set of building units with well-defined geometry are less likely to form interpenetrated structures in topologies that only allow for the formation of hetero-dual nets. The **nbo** net can however interpenetrate and form a self-dual net, if the origin of the second framework is not positioned at the center of the tile of the original net. Thus, a careful analysis of the net topology is required to determine whether interpenetration is likely to occur, or not.

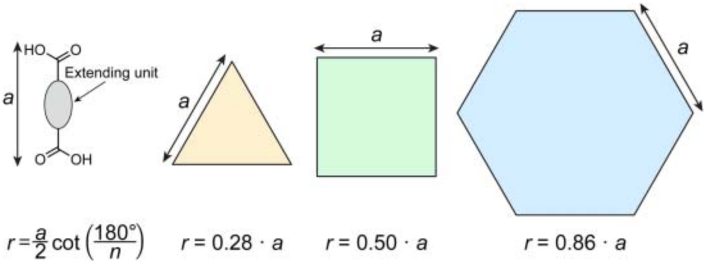

Figure 2.10 Geometric consideration of the relation between the number of edges (n) of an n-sided polygon, the length a of the edges, and the radius r of the inscribed circle. The radius of the inscribe circle of polygons with n sides of a given length a becomes larger the more edges the polygon has. In the context of reticular chemistry this means that the same linker can afford the formation of various pore sizes depending on the geometry of the pore.

Toward this end efforts were made to expand the pore size of many MOFs into the mesoporous regime. The isoreticular expansion of MOF-74, which is a MOF built from 1D rod SBUs connected by linear H_4DOT (DOT = 2,5-dioxidoterephthalate) linkers forming a structure with 1D hexagonal channels is promising, especially since its **etb** topology is unlikely to interpenetrate because of its hetero-dual nature (Figure 2.11).

The preparation and characterization of an isoreticular MOF-74 series constructed from linkers ranging from 7 to 50 Å and having pore diameters ranging from 14 × 10 to 85 × 98 Å is illustrated in Figure 2.12a [24]. To achieve pore sizes of this magnitude many challenges have to be overcome: (i) the design of the organic linkers, (ii) their synthesis in pure form, and (iii) ultimately the crystallization of the resulting isoreticular expanded MOFs. Long chains of p-linked aryl units, however, are generally poorly soluble due to strong π–π stacking interactions. The solubility of the starting materials is a necessary requirement

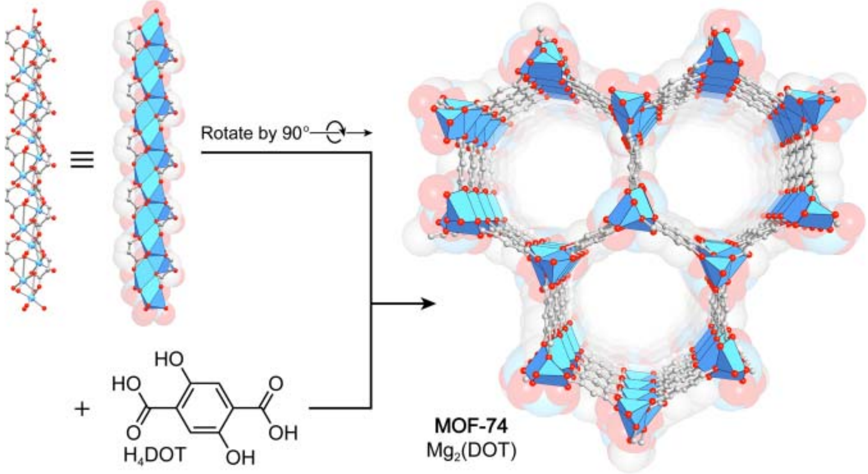

Figure 2.11 Crystal structure of MOF-74. Linking 1D rod SBUs by linear DOT linkers affords the formation of a framework of **etb** topology. The structure resembles that of a honeycomb with 1D channels running along the crystallographic *c*-axis. The coordination sphere of the metal centers in the SBUs is completed by one neutral water ligand per metal center that can be removed to afford the generation of open metal sites. All hydrogen atoms and terminal water ligands in the structure of MOF-74 are omitted for clarity. The structure is superimposed onto its own space filling model. Color code: Zn, blue; C, gray; O, red.

for the crystallization of MOFs, hence aliphatic side chains engendering a torsional twist between the planes of the rings are introduced, thereby reducing π–π stacking interactions. The series of palindromic oligophenylene derivatives terminated with α-hydroxy-carboxylic acid functionalities based on the H$_4$DOT linker of MOF-74 used to prepare members of the IRMOF-74 series are given in Figure 2.12b.

In structures with 3D spherical pores, the cross-section of the cages confining these pores often consists of polygons with a large number of edges (n), which allows for the formation of large 3D pores from relatively short linkers. MIL-100 is an ideal starting point for the isoreticular expansion of a MOF with 3D pores following the principles outlined earlier. The structure of this MOF comprises large cages with pore diameters of 25 and 29 Å, built from supertetrahedral tertiary building units (TBUs), that are joined to form an extended structure based on the **mtn** topology, a hetero-dual net [25]. Replacing the 1,3,5-benzenetricarboxylate (BTC) linker in MIL-100 by an expanded analog (i.e. BTB) results in the formation of MIL-100(Fe_BTB). Theoretical pore sizes of 55 and 68 Å were calculated from crystal structure data since the nonplanar BTB linker induces stress into the framework rendering the activation of this difficult [26]. Thus, two completely planar linkers, BTTC and TATB, are used to prepare another two isoreticular expanded analogs of MIL-100, termed PCN-332 and PCN-333, respectively (Figure 2.13) [27]. These materials are architecturally stable and their pore sizes were determined experimentally after activation. In these MOFs, the cages are expanded from 25 and 29 Å in MIL-100, to 34 and 45 Å in PCN-332 and 55 and 68 Å in PCN-333. PCN-333 has the largest

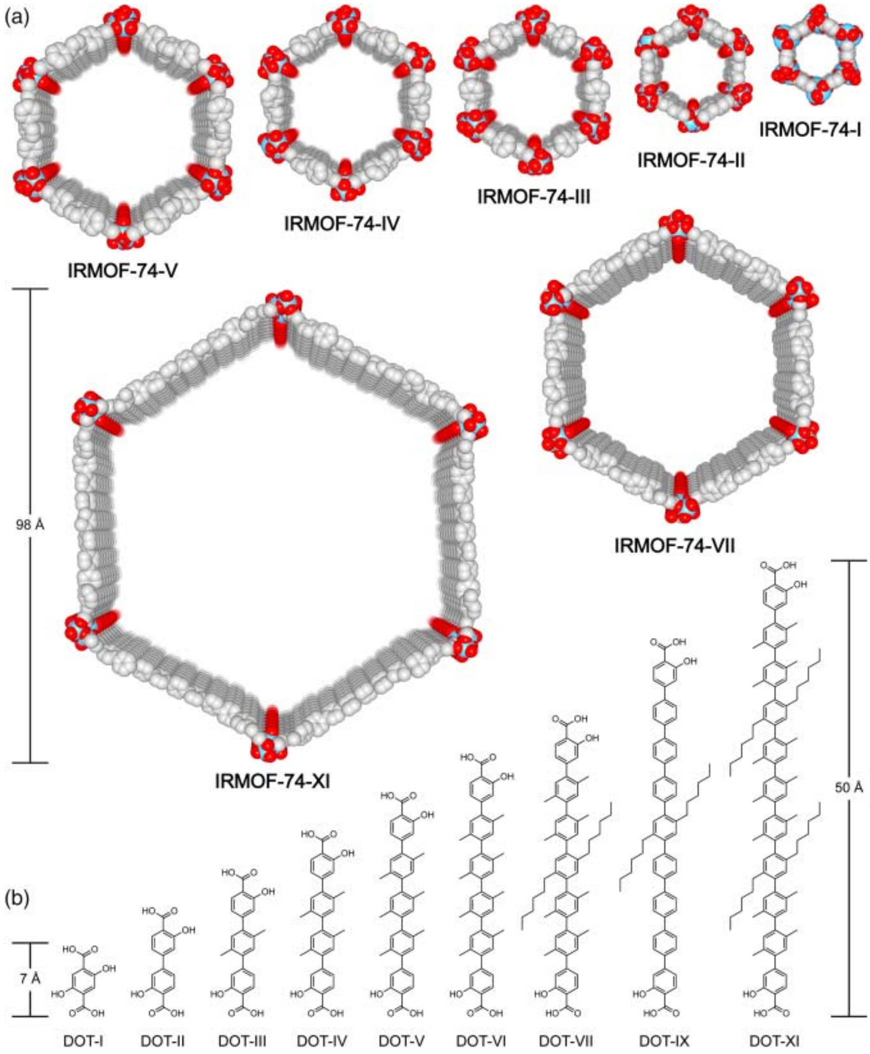

Figure 2.12 (a) Isoreticular series of MOFs with **etb** topology. By successive elongation of the palindromic DOT linker pore sizes of up to 98 Å are achieved. The space filling model of selected members of the IRMOF-74 is shown. (b) Palindromic linkers with terminal hydroxybenzoic acid groups used to prepare members of the IRMOF-74 series. The aliphatic side chains result in a torsional twist of the linkers, rendering them more soluble due to reduced π–π stacking interactions. In the crystal structure drawings all alkyl side chains and hydrogen atoms are omitted for clarity. Color code: Zn, blue; C, gray; O, red.

accessible cages in permanently porous carboxylate-based MOFs reported to date, making it an interesting candidate for trapping large molecules such as enzymes. This example highlights the power of the isoreticular principle for tailoring pore metrics [27]. It is important to mention that the presence of large pores does not necessarily translate into high surface areas as discussed in Section 2.4.2.

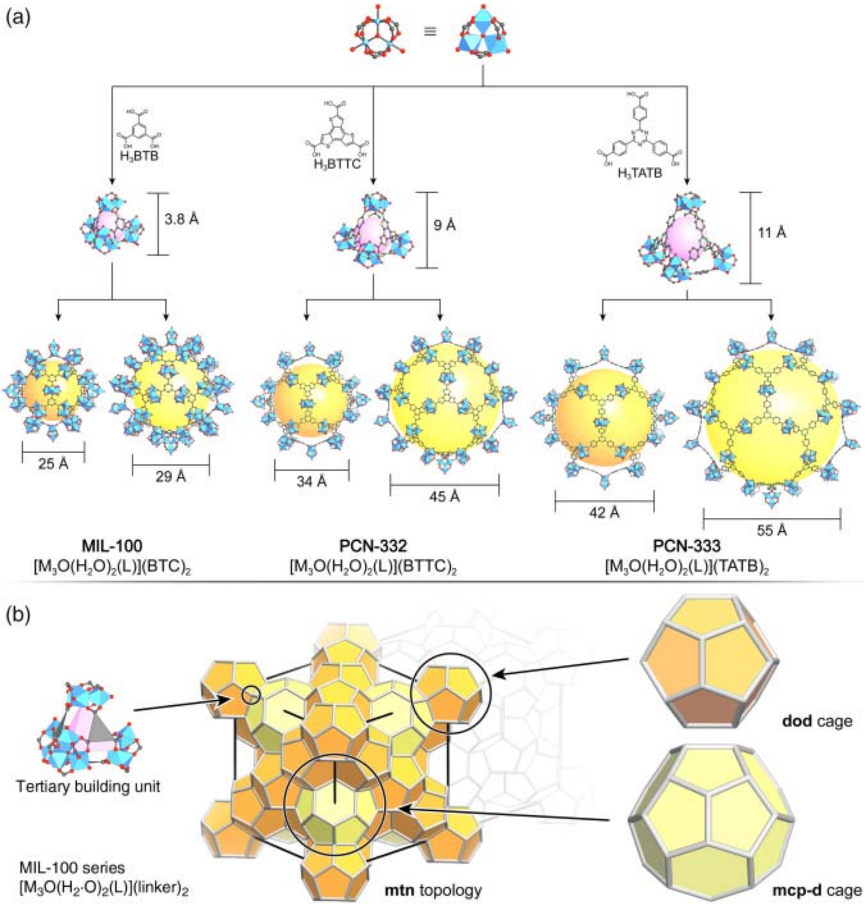

Figure 2.13 (a) Formation of three types of cage by reticulation of 6-c $M_3OL_3(\text{–}COO_2)_6$ SBUs and trigonal tritopic linkers. Increasing the size of the tritopic BTC linker used to prepare MIL-100 while maintaining its D_{3h} symmetry affords the formation of PCN-332 and PCN-333 with pore sizes of up to 55 Å. All structures contain two different types of cage with **dod** and **mcp-d** topology, shown in orange and yellow, respectively. (b) Deconstruction of the **mtn** topology of the MIL-100 series MOFs. Tetrahedral tertiary building units (TBUs) are formed by linking four $M_3OL_3(\text{–}COO_2)_6$ SBUs through trigonal tritopic linkers. These TBUs are further linked in a vertex sharing manner to give cages of **dod** (orange) and **mcp-d** topology (yellow) that eventually are fused into an extended structure of **mtn** topology. All hydrogen atoms are omitted for clarity. Color code: Cr, blue; C, gray; N, green; O, red.

2.4.2 Ultrahigh Surface Area

Even though PCN-333 has the largest cages in carboxylate-based MOFs reported to date, it has a comparatively low surface area of 4000 $m^2\ g^{-1}$. For comparison, MOF-5 has pores with a diameter of only 15.1 Å but a surface area of 3800 $m^2\ g^{-1}$. This illustrates that there is no direct correlation between the pore size and the surface area. As discussed earlier, the gas uptake in the low-pressure region, which is more relevant for practical applications, is mostly determined by the accessible surface area and not the pore size. Therefore, with respect to the gas adsorption-based applications, the development of materials with ultrahigh surface areas is of interest (see Chapters 14–17). In the following text we illustrate parameters that determine the surface area with respect to gas adsorption, and outline principles that specifically help design MOFs with ultrahigh surface areas.

The first step in understanding how to achieve high surface areas is to identify the adsorption sites in MOFs and to maximize their numbers (Figure 2.14). In general, the major adsorption sites are found in the vicinity of the SBU. They are preferred due to the polar nature of the SBU and the resulting strong interactions with the adsorbate. Additional adsorption sites are located close to the organic linker, more precisely on the faces and the edges of the aryl units, highlighting the role of the linker in the design of materials with large accessible surface areas. The adsorption sites for argon and nitrogen in MOF-5 shown in Figure 2.14 were determined by X-ray diffraction at 30 K and later corroborated by inelastic neutron diffraction, Raman measurements, and theoretical studies [28].

The binding of adsorbed gas molecules to the inner surface of MOFs is stronger than in carbon-based materials. Experiments and calculations suggest that in MOFs, the strength of interactions with the framework is further enhanced by the use of more polarizing centers or by the presence of open metal sites [28c]. The strength of an interaction of a gas molecule adsorbed on a surface is approximated

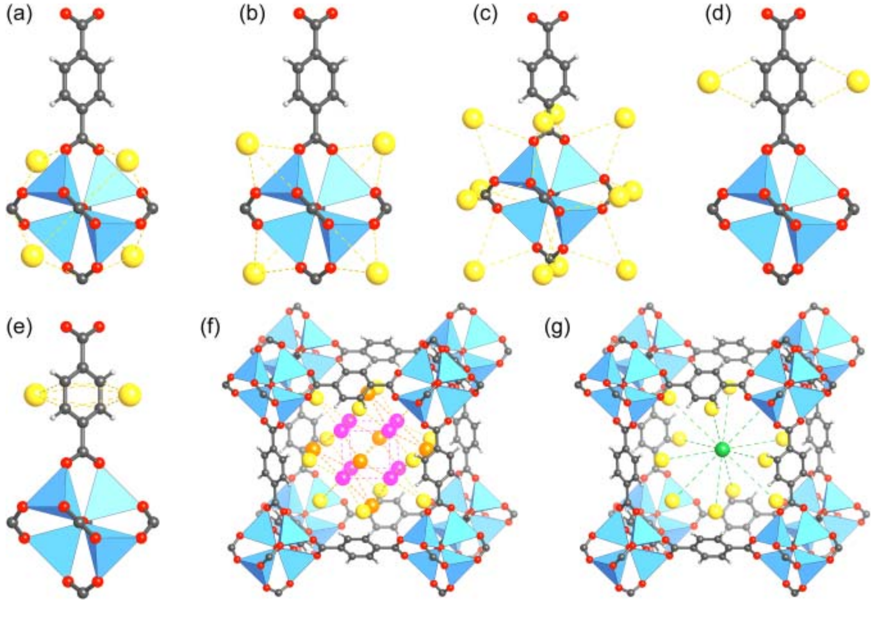

Figure 2.14 Adsorption sites of argon in MOF-5 determined by X-ray diffraction at 30 K, eight symmetry-independent sites were crystallographically identified. (a–c) Gas molecules are preferentially adsorbed close to the polar SBU. (d, e) Additional adsorption sites are located on the edges and faces of the organic linker. (f) A second layer is formed in the large pore of MOF-5 (pink and orange spheres), and (g) one additional adsorption site is found in the center of the small pore (green sphere). Color code: Zn, blue; C, gray; O, red; adsorbed Ar, yellow/orange/pink/green.

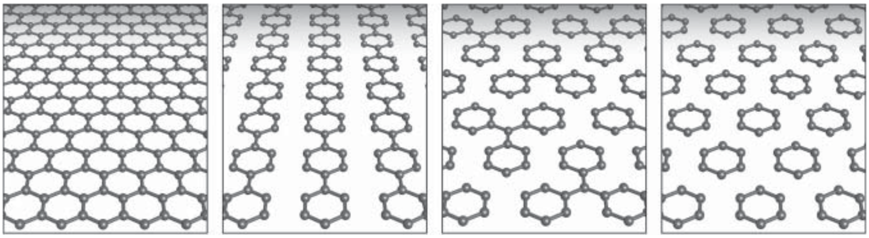

Figure 2.15 A strategy to maximize the number of adsorption sites and surface area of MOFs by designing linkers with a maximized number of exposed faces and edges. Trigonal 1,3,5-triphenyl benzene-based linkers provide a high number of exposed adsorption sites while still allowing for both, isoreticular expansion and functionalization.

by measuring its rotational barrier near that surface using inelastic neutron scattering. Such measurements were carried out on MOF-5 as a function of hydrogen pressure, revealing that hydrogen is bound strongly to its SBU, whereas the interaction with additional adsorption sites on the faces and edges of the aryl units of the linkers is comparatively weak. Nevertheless, these adsorption sites still play a key role in enhancing the gas uptake in MOFs because their numbers can be deliberately maximized by optimizing the shape and metrics of the linker.

This is illustrated by the following theoretical exercise (Figure 2.15). Starting from a simple graphene sheet the number of exposed edges is increased by forming smaller polymeric or molecular subunits. A single infinite graphene sheet has a theoretical surface area of 2965 $m^2\ g^{-1}$, which is increased to 5683 $m^2\ g^{-1}$ for the case of infinite chains of poly-*p*-linked benzene, as more edges are exposed. Dividing the graphene sheet into 1,3,5-triphenylbenzene units increases the theoretical surface area even further (6200 $m^2\ g^{-1}$) and maximizing the number of exposed edges by forming isolated benzene rings results in a theoretical surface area of 7745 $m^2\ g^{-1}$. Since in the case of isolated benzene rings attaching binding groups significantly lowers the number of adsorption sites, it seems most promising to employ trigonal 1,3,5-triphenylbenzene based linkers when targeting ultrahigh surface areas, as they provide the maximum number of faces and edges while still allowing for the synthesis of framework structures and their isoreticular expansion [29].

This strategy was implemented by reticulating 1,3,5-benzenetribenzoate (H_3BTB) and basic zinc carboxylate clusters ($Zn_4O(COO)_6$) to form MOF-177, a MOF of **qom**[3] topology. In contrast to other net topologies constructed from nodes of a similar general geometry (octahedron and triangle), such as the default **pyr** net (self-dual net), frameworks of **qom** topology (hetero-dual net) are not prone to interpenetration. Thus, the structure of MOF-177 is non-interpenetrated and its BET surface area is 4500 $m^2\ g^{-1}$ despite the relatively small pores (~12 Å) [29].

Calculations suggest that linkers containing cumulene (=C=C=) and polyyne (—C≡C—) units have even higher specific surface areas (up to 14 937 $m^2\ g^{-1}$, presumably the highest possible specific surface area) than those built only from

---

[3] **qom** = Queen of MOF. This name was chosen since it was thought that this topology will allow for the highest surface area possible.

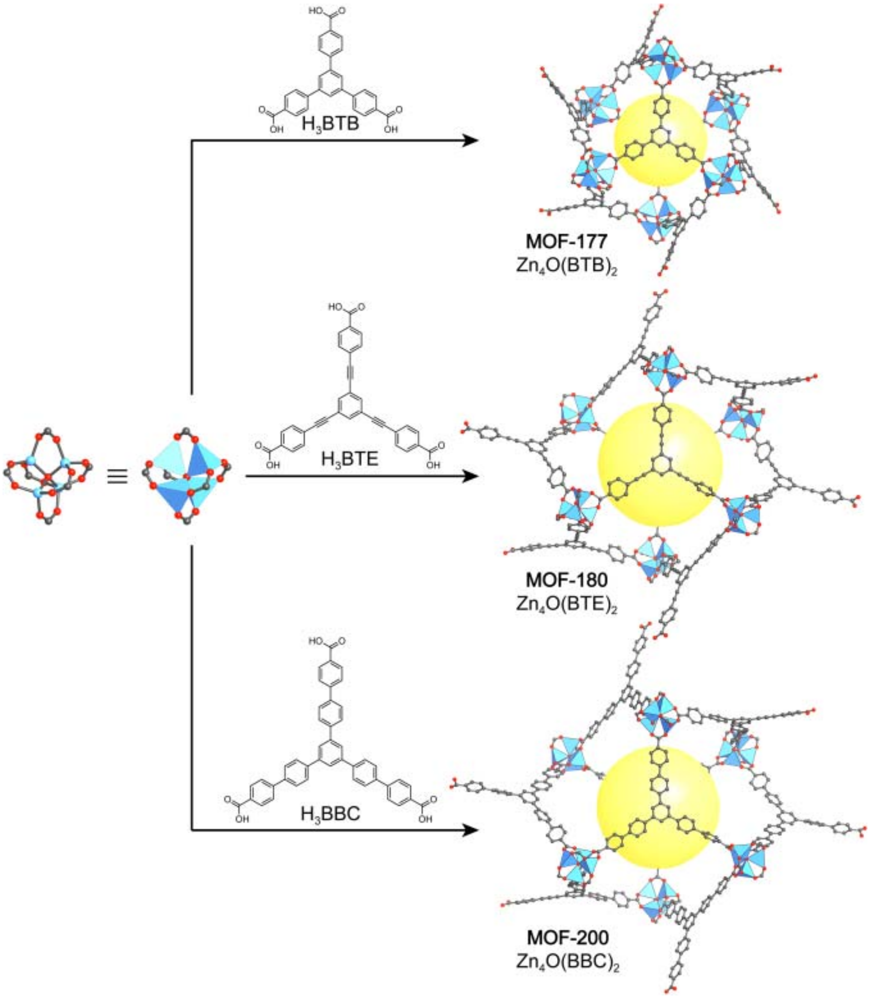

Figure 2.16 Isoreticular series of MOFs with **qom** topology formed by reticulation of trigonal tritopic linkers (H_3BTB, H_3BTE, and H_3BBC) and octahedral $Zn_4O(–COO)_6$ SBUs. (a) MOF-177, (b) MOF-180, and (c) MOF-200 have geometric surface areas of 4740, 6080, and 6400 $m^2\ g^{-1}$, respectively. The **qom** net is a hetero-dual net, hence no interpenetration is observed when expanded linkers are used. All hydrogen atoms are omitted for clarity. Color code: Zn, blue; C, gray; O, red.

aryl units. Therefore, elongated linkers derived from BTB with additional alkynyl (BTE) or aryl units (BBC) were designed to synthesize an isoreticular series of MOFs based on MOF-177 (Figure 2.16). The resulting frameworks, MOF-180 and MOF-200, have calculated porosities of 89% and 90%, respectively. The highly porous structures of these MOFs made it difficult or, as in the case of MOF-180, even impossible to activate them, which is the reason why the reported BET surface area for MOF-200 (4530 $m^2\ g^{-1}$) is far lower than what is expected from geometrical calculations (6400 $m^2\ g^{-1}$) [30].

These principles of linker design allow to conceive MOFs with even higher surface areas. We will illustrate this for an isoreticular series of MOFs with **ntt** topology (equivalent to **rht** topology, see Section 5.2.3). The parent MOF to this series is PMOF-1 ($Cu_3(H_2O)$(TPBTM)), which has a surface area of 3160 m^2 g^{-1} [31]. Isoreticular expansion using HTTEI linkers affords $Cu_3(H_2O)$(TTEI), which is referred to as both, PCN-610 and NU-100 [32].[4] The activation of this MOF is challenging but eventually affords a material with a surface are of 6143 m^2 g^{-1}. To reach even higher surface areas the linker used to prepare NU-100 is expanded even further (BHEHPI) yielding NU-110, which after activation has a surface area of 7140 m^2 g^{-1} [33]. The isoreticular series of **ntt** MOFs alongside the linkers used to prepare them is given in Figure 2.17. Note that the linker design is based on the principles discussed earlier.

The expansion of the octahedral pore (19 Å) in PMOF-1 by a factor of 39% (26 Å for PCN-610) results in a 94% larger surface area whereas further increase in pore size by another 26% (33 Å in NU-110) only leads to a 16% higher surface area. This highlights that there is no direct correlation between pore size and surface area and that above a certain diameter, large pores partially consist of "dead volume" where the adsorbate does not interact with the surface of the pore. Another disadvantage of large pores when targeting MOFs with good sorption properties is the fact that while the gravimetric gas uptake (m^2 g^{-1}) might be high a low volumetric uptake (m^2 cm^{-3}) is inevitable. The gravimetric uptake increases with the pore size until the theoretical limit is reached. In contrast, the volumetric uptake will only increase until a critical pore size is reached and will decrease upon further expansion.

We illustrate this based on an isoreticular expansion of a hypothetical MOF of **pcu** topology (Figure 2.18). In structures of this topology, the geometric surface area can be estimated as a sphere where all parts of the spherical surface that are not covered by the framework structure are subtracted, as they do not contribute to the surface area. Upon expansion, these areas occupy a continuously growing part of the spherical surface, hence the effective surface area does not grow at a constant rate. The infinitely expanded structure can be approximated to consist only of chains of poly-*p*-linked benzene rings and its molecular mass can therefore be approximated by that of poly(*p*-phenylene). From this point on no further gain in surface area per weight will be observed according to this model, and the theoretical limit of 6200 m^2 g^{-1} is reached (green line in Figure 2.18) [34]. This is different when analyzing the surface area per volume, which will reach a maximum before the decrease in density outweighs the increase in surface area resulting in a decrease of the surface area per volume upon further expansion of the framework (blue line in Figure 2.18).

This behavior is also important in considering practical applications and it must be pointed out that all effects mentioned above are strongly dependent on the nature and size of the adsorbent in question. Therefore, the structures of MOFs have to be carefully designed, examined, and modified in order to create

---

[4] This MOF was reported by two groups simultaneously and therefore has two different names.

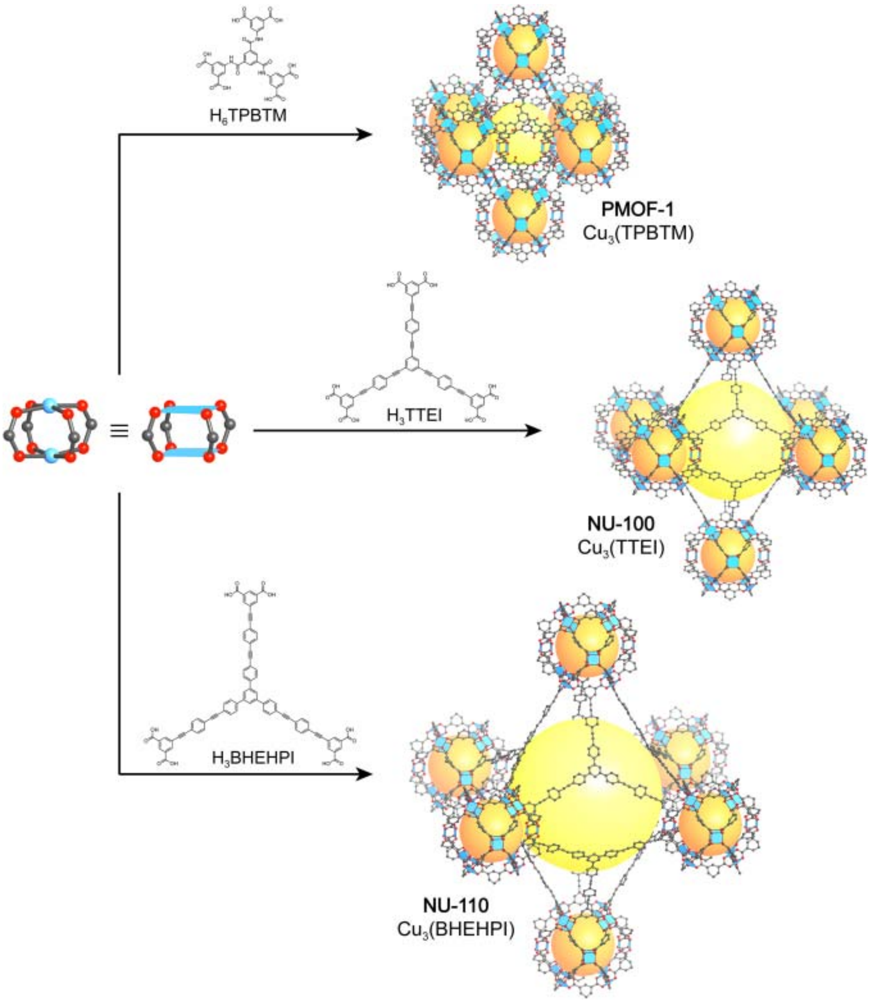

Figure 2.17 Isoreticular series of MOFs with **ntt** topology formed by reticulation of trigonal hexatopic linkers (H_6TPBTM, H_6TTEI, and H_6BHEHPI) and square 4-c $Cu_2(–COO)_4$ paddle wheel SBUs. (a) PMOF-1, (b) NU-100, and (c) NU-110 have surface area of 3160, 6143, and 7140 $m^2\ g^{-1}$, respectively. The **ntt** net is a hetero-dual net and therefore unlikely to interpenetrate. The terminal *m*-BDC moieties of the hexatopic linker connect the SBUs to form 24-c tertiary building units of **rco** topology. These cages maintain their size upon isoreticular expansion and only the large pore located in the octahedral hole formed by the TBUs increases in size. All hydrogen atoms as well as all terminal water ligands on the paddle wheel SBUs are omitted for clarity. Color code: Zn, blue; C, gray; N, green; O, red.

high-performance materials with outstanding properties. Over the past years the number of reported MOF structures increased exponentially, and efforts were made to simplify and systemize their structures to understand how to use reticular chemistry as a means to construct extended structures by design and this will be the focus of the Chapters 3–6.

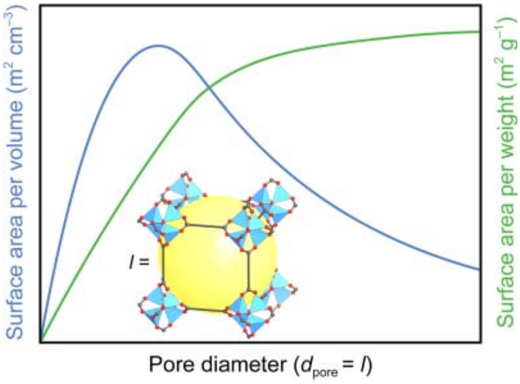

Figure 2.18 Schematic plot of the surface area per volume (blue) and per weight (green) versus the pore diameter. The change in surface area is based on a simplified cubic model system with a linker of variable length *l*. For very long linkers, the molecular mass of the compound is approximately that of poly(*p*-phenylene) since the contribution of the SBUs is considered to be negligible. The surface area per mass can therefore also be approximated by that of poly(*p*-phenylene). In contrast, the surface per volume passes through a maximum before the decrease in density outweighs the increase in surface area.

2.5 Summary

In this chapter we introduced the terminology used to describe porous materials. We showed the process of gas adsorption, the resulting types of isotherms and hysteresis, and the interactions that can be involved in this process. Based on these considerations we outlined the theory of gas adsorption in porous solids and discussed the two models most frequently used to describe it: the Langmuir and the BET-model. The different assumptions used to derive these models allow to understand their applicability to MOFs and specific types of measurements. With the isoreticular principle we provided a tool for the design MOFs with large pores and predefined topology and examples making use of this principle were given. We showed that there is no direct correlation between the pore size and the surface area and consequently introduced design principles for the targeted synthesis of new MOFs with ultrahigh surface areas alongside illustrative examples. In Chapter 3 we will introduce the building units of MOFs – organic linkers and inorganic SBUs – and general synthetic approaches to their synthesis.

References

1 (a) Cronstedt, A.F. (1756). Rön och beskrifning om en obekant bärg art, som kallas Zeolites. *Svenska Vetenskaps akademiens Handlingar* 17: 120. A translation can be found in Schlenker, J.L. and Kühl, G.H. (1993). *Proc. 9th Intl. Conference on Zeolites.* (b) Claire-Deville, H.d.S. (1862). Reproduction de la levyne. *Comptes Rendus* 54 (1862): 324–327. (c) Friedel, G. (1896). New experiments on zeolites. *Bulletin de la Societe Francaise de Mineralogie* 19: 363–390. (d) Friedel, G. (1896). Sur quelques propriétés nouvelles des zéolithes. *Bulletin de la Société Française de Minéralogie* 19: 94–118. (e) Barrer, R.M. (1938). The sorption of polar and non-polar gases by zeolites. *Proceedings of the Royal Society of London Series A: Mathematical and Physical Sciences* 167 (A930): 0392–0420. (f) Barrer, R.M. (1949). Transient flow of gases in sorbents providing uniform capillary networks of molecular dimensions. *Transactions of the Faraday Society* 45 (4): 358–373. (g) Barrer, R.M. and Macleod, D.M. (1954). Intercalation and sorption by montmorillonite. *Transactions of the Faraday Society* 50 (9): 980–989.

2 (a) Baerlocher, C., McCusker, L.B., and Olson, D.H. (2007). *Atlas of Zeolite Framework Types*. Elsevier. (b) Corma, A., Díaz-Cabañas, M.J., Jiang, J. et al. (2010). Extra-large pore zeolite (ITQ-40) with the lowest framework density containing double four- and double three-rings. *Proceedings of the National Academy of Sciences of the United States of America* 107 (32): 13997–14002. (c) Kulprathipanja, S. (ed.) (2010). *Zeolites in Industrial Separation and Catalysis*, 1–26. Wiley.

3 Schaeffer, W.D., Dorsey, W.S., Skinner, D.A., and Christian, C.G. (1957). Separation of xylenes, cymenes, methylnaphthalenes and other isomers by clathration with inorganic complexes. *Journal of the American Chemical Society* 79 (22): 5870–5876.

4 Soldatov, D.V., Enright, G.D., and Ripmeester, J.A. (2004). Polymorphism and pseudopolymorphism of the [Ni(4-methylpyridine)$_4$(NCS)$_2$] Werner complex, the compound that led to the concept of "organic zeolites". *Crystal Growth & Design* 4 (6): 1185–1194.

5 Allison, S.A. and Barrer, R.M. (1969). Sorption in the β-phases of transition metal(II) tetra-(4-methylpyridine)thiocyanates and related compounds. *Journal of the Chemical Society A: Inorganic, Physical, Theoretical* 1717–1723.

6 Krap, C.P., Balmaseda, J., Zamora, B., and Reguera, E. (2010). Hydrogen storage in the iron series of porous Prussian blue analogues. *International Journal of Hydrogen Energy* 35 (19): 10381–10386.

7 Ramprasad, D., Pez, G.P., Toby, B.H. et al. (1995). Solid state lithium cyanocobaltates with a high capacity for reversible dioxygen binding: synthesis, reactivity, and structures. *Journal of the American Chemical Society* 117 (43): 10694–10701.

8 Kondo, M., Yoshitomi, T., Matsuzaka, H. et al. (1997). Three-dimensional framework with channeling cavities for small molecules: $\{[M_2(4,4'\text{-bpy})_3(NO_3)_4]\cdot xH_2O\}_n$ (M = Co, Ni, Zn). *Angewandte Chemie International Edition in English* 36 (16): 1725–1727.

9 (a) Takamizawa, S., Mori, W., Furihata, M. et al. (1998). Synthesis and gas-occlusion properties of dinuclear molybdenum(II) dicarboxylates (fumarate, terephthalate, trans-trans-muconate, pyridine-2,5-dicarboxylate, and trans-1,4-cyclohexanedicarboxylate). *Inorganica Chimica Acta* 283 (1): 268–274. (b) Mori, W., Hoshino, H., Nishimoto, Y., and Takamizawa, S. (1999). Synthesis and gas occlusion of new micropore substance rhodium(II) carboxylates bridged by pyrazine. *Chemistry Letters* 28 (4): 331–332. (c) Wasuke, M., Fumie, I., Keiko, Y. et al. (1997). Synthesis of new adsorbent copper(II) terephthalate. *Chemistry Letters* 26 (12): 1219–1220.

10 Li, H., Eddaoudi, M., Groy, T.L., and Yaghi, O.M. (1998). Establishing microporosity in open metal-organic frameworks: gas sorption isotherms for Zn(BDC) (BDC = 1,4-benzenedicarboxylate). *Journal of the American Chemical Society* 120 (33): 8571–8572.

11 Li, H., Eddaoudi, M., O'Keeffe, M., and Yaghi, O.M. (1999). Design and synthesis of an exceptionally stable and highly porous metal-organic framework. *Nature* 402 (6759): 276–279.

12 (a) Kayser, H. (1881). Wiederman's. *Annals of Physical Chemistry* 14: 451. (b) Kayser, H. (1881). Über die verdichtung von gasen an oberflächen in ihrer abhängigkeit von druck und temperatur. *Annalen der Physik* 250 (11): 450–468. (c) Everett, D. (1972). Manual of symbols and terminology for physicochemical quantities and units, appendix II: definitions, terminology and symbols in colloid and surface chemistry. *Pure and Applied Chemistry* 31 (4): 577–638.

13 McBain, J.W. (1909). XCIX. The mechanism of the adsorption ("sorption") of hydrogen by carbon. *The London, Edinburgh, and Dublin Philosophical Magazine and Journal of Science* 18 (108): 916–935.

14 (a) Sing, K.S. (1985). Reporting physisorption data for gas/solid systems with special reference to the determination of surface area and porosity (Recommendations 1984). *Pure and Applied Chemistry* 57 (4): 603–619. (b) Wilkinson, A. and McNaught, A. (1997). *IUPAC Compendium of Chemical Terminology, (The "Gold Book")*. International Union of Pure and Applied Chemistry.

15 (a) Brunauer, S., Emmett, P.H., and Teller, E. (1938). Adsorption of gases in multimolecular layers. *Journal of the American Chemical Society* 60 (2): 309–319. (b) Brunauer, S., Deming, L.S., Deming, W.E., and Teller, E. (1940). On a theory of the van der Waals adsorption of gases. *Journal of the American Chemical Society* 62 (7): 1723–1732. (c) Brunauer, S. (1945). *The Adsorption of Gases and Vapours*, vol. 1. Oxford: Oxford University Press.

16 (a) Broekhoff, J. (1979). Mesopore determination from nitrogen sorption isotherms: fundamentals, scope, limitations. *Studies in Surface Science and Catalysis* 3: 663–684. (b) Lowell, S., Shields, J.E., Thomas, M.A., and Thommes, M. (2012). *Characterization of Porous Solids and Powders: Surface Area, Pore Size and Density*, vol. 16. Springer Science & Business Media. (c) Thommes, M., Kaneko, K., Neimark, A.V. et al. (2015). Physisorption of gases, with special reference to the evaluation of surface area and pore size distribution (IUPAC Technical Report). *Pure and Applied Chemistry* 87 (9–10): 1051–1069.

17 Langmuir, I. (1918). The adsorption of gases on plane surfaces of glass, mica and platinum. *Journal of the American Chemical Society* 40 (9): 1361–1403.

18 Langmuir, I. (1916). The evaporation, condensation and reflection of molecules and the mechanism of adsorption. *Physical Review* 8 (2): 149–176.

19 (a) Everett, D.H. (1950). Thermodynamics of adsorption. Part I. General considerations. *Transactions of the Faraday Society* 46: 453–459. (b) Everett, D.H. (1950). The thermodynamics of adsorption. Part II. Thermodynamics of monolayers on solids. *Transactions of the Faraday Society* 46: 942–957.

20 Gomez-Gualdron, D.A., Moghadam, P.Z., Hupp, J.T. et al. (2016). Application of consistency criteria to calculate BET areas of micro- and mesoporous metal-organic frameworks. *Journal of the American Chemical Society* 138 (1): 215–224.

21 Eddaoudi, M., Kim, J., Rosi, N. et al. (2002). Systematic design of pore size and functionality in isoreticular MOFs and their application in methane storage. *Science* 295 (5554): 469–472.

22 Reineke, T.M., Eddaoudi, M., Moler, D. et al. (2000). Large free volume in maximally interpenetrating networks: the role of secondary building units exemplified by $Tb_2(ADB)_3[(CH_3)_2SO]_4{\cdot}16[(CH_3)_2SO]^1$. *Journal of the American Chemical Society* 122 (19): 4843–4844.

23 Delgado-Friedrichs, O. and O'Keeffe, M. (2005). Crystal nets as graphs: terminology and definitions. *Journal of Solid State Chemistry* 178 (8): 2480–2485.

24 Deng, H., Grunder, S., Cordova, K.E. et al. (2012). Large-pore apertures in a series of metal-organic frameworks. *Science* 336 (6084): 1018–1023.

25 Ferey, G., Serre, C., Mellot-Draznieks, C. et al. (2004). A hybrid solid with giant pores prepared by a combination of targeted chemistry, simulation, and powder diffraction. *Angewandte Chemie International Edition* 43 (46): 6296–6301.

26 Horcajada, P., Chevreau, H., Heurtaux, D. et al. (2014). Extended and functionalized porous iron(iii)tri-or dicarboxylates with MIL-100/101 topologies. *Chemical Communications* 50 (52): 6872–6874.

27 Feng, D., Liu, T.-F., Su, J. et al. (2015). Stable metal-organic frameworks containing single-molecule traps for enzyme encapsulation. *Nature Communications* 6: 5979.

28 (a) Rowsell, J.L.C., Spencer, E.C., Eckert, J. et al. (2005). Gas adsorption sites in a large-pore metal-organic framework. *Science* 309 (5739): 1350–1354. (b) Rowsell, J.L., Eckert, J., and Yaghi, O.M. (2005). Characterization of H_2 binding sites in prototypical metal-organic frameworks by inelastic neutron scattering. *Journal of the American Chemical Society* 127 (42): 14904–14910. (c) Centrone, A., Siberio-Perez, D.Y., Millward, A.R. et al. (2005). Raman spectra of hydrogen and deuterium adsorbed on a metal-organic framework. *Chemical Physics Letters* 411 (4–6): 516–519. (d) Dubbeldam, D., Frost, H., Walton, K.S., and Snurr, R.Q. (2007). Molecular simulation of adsorption sites of light gases in the metal-organic framework IRMOF-1. *Fluid Phase Equilibria* 261 (1): 152–161. (e) Greathouse, J.A., Kinnibrugh, T.L., and Allendorf, M.D. (2009). Adsorption and separation of noble gases by IRMOF-1: grand canonical Monte Carlo simulations. *Industrial and Engineering Chemistry Research* 48 (7): 3425–3431.

29 Chae, H.K., Siberio-Pérez, D.Y., Kim, J. et al. (2004). A route to high surface area, porosity and inclusion of large molecules in crystals. *Nature* 427 (6974): 523–527.

30 Furukawa, H., Ko, N., Go, Y.B. et al. (2010). Ultrahigh porosity in metal-organic frameworks. *Science* 329 (5990): 424–428.

31 Zheng, B., Bai, J., Duan, J. et al. (2010). Enhanced CO_2 binding affinity of a high-uptake rht-type metal-organic framework decorated with acylamide groups. *Journal of the American Chemical Society* 133 (4): 748–751.

32 (a) Yuan, D., Zhao, D., Sun, D., and Zhou, H.C. (2010). An isoreticular series of metal-organic frameworks with dendritic hexacarboxylate ligands and exceptionally high gas-uptake capacity. *Angewandte Chemie International Edition* 49 (31): 5357–5361. (b) Farha, O.K., Yazaydin, A.O., Eryazici, I. et al. (2010). De novo synthesis of a metal-organic framework material featuring ultrahigh surface area and gas storage capacities. *Nature Chemistry* 2 (11): 944–948.

33 Farha, O.K., Eryazici, I., Jeong, N.C. et al. (2012). Metal-organic framework materials with ultrahigh surface areas: is the sky the limit? *Journal of the American Chemical Society* 134 (36): 15016–15021.

34 Schnobrich, J.K., Koh, K., Sura, K.N., and Matzger, A.J. (2010). A framework for predicting surface areas in microporous coordination polymers. *Langmuir* 26 (8): 5808–5814.